Improvement of protective oxide layers formed by high-frequency plasma electrolytic oxidation on Mg-RE alloy with LPSO-phase

Alisa O. Cheretaeva [a] *, Pavel A. Glukhov [a], Marat R. Shafeev [a], Alyona G. Denisova [a], Eugeny D. Borgardt [a], Anton V. Polunin [a], Alexander V. Katsman [ab], Mikhail M. Krishtal [a]

a: Institute of Advanced Technologies, Togliatti State University, Togliatti 445020, Russia
b: Department of Materials Science and Engineering, Technion – Israel Institute of Technology, Haifa 32000, Israel
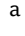***** Corresponding author: a.cheretaeva@tltsu.ru

This paper belongs to a Regular Issue.

Abstract

Oxide layers on $Mg_{97}Y_2Zn_1$ magnesium alloy with strengthening LPSO-phase were formed by plasma electrolytic oxidation (PEO) in bipolar mode with frequency variation of forming current pulses (50 and 500 Hz) and addition of sodium aluminate or sodium silicate to alkali phosphate fluoride electrolyte. Microstructure, chemical and phase composition, corrosion and mechanical properties of the oxide layers formed were investigated. With increasing current frequency for both electrolytes, an increase in homogeneity of the oxide layers structure and a decrease in their porosity and fracturing at constant thickness were recorded. The oxide layers formed at 500 Hz even with some decrease in hardness have better adhesive strength and 2 orders of magnitude higher short-term corrosion resistance values. PEO of Mg-alloy with LPSO-phase in the electrolyte with addition of sodium aluminate in combination with increased pulse frequency (500 Hz) allows forming the best-quality uniform oxide layer with high hardness, adhesive strength and corrosion resistance properties. The use of electrolyte with addition of sodium silicate reduced the adhesive strength by 1.5 times and brought down the long-term corrosion resistance of oxide layers by an order of magnitude, as compared with the electrolyte with sodium aluminate. The reason for a significant improvement in the complex of protective properties of the oxide layers with an increase in the current pulse frequency is supposed to be a decrease in the power and duration of individual microarc discharges with simultaneous increase in their number per unit oxidized area.
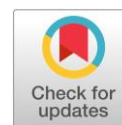
Key findings

● PEO of Mg-RE (LPSO) alloy allows improving its corrosion behaviour and surface mechanical properties.

● Increase of pulse frequency under PEO allows decreasing the porosity and heterogeneity of the oxide layers.

● The best corrosion resistance and adhesive strength demonstrate the oxide layer obtained in aluminate electrolyte under high-frequency PEO.

1. Introduction

Magnesium alloys have great potential for different industrial applications due to their high specific strength, damping ability and good workability [1–4]. Main disadvantages that prevent wide application of Mg alloys in aviation and aerospace industry are low ignition temperature and high fire hazard, absolute mechanical strength deficiency and insufficient corrosion resistance [5–8]. In the past decade, considerable progress has been made in the development of zinc-containing magnesium alloys with rare earth elements (Mg–RE), which, at a certain Zn ratio, can form alloys with a long-period stacking-ordered structure (LPSO-phase) [9–12]. Compared to conventional Mg alloys with dispersion strengthening, the eutectic structures of these alloys after thermal treatment are trans-

formed into LPSO-phases shaped as thin plates with 1.5 to 25 nm thickness [13]. They significantly increase the static and fatigue strength, ductility and thermal stability of the alloy. LPSO-phase formed from various combinations of Mg, Zn, Y, etc., prevents the movement of dislocations and reduces the anisotropy of the material properties, whereby high mechanical performance is achieved [14, 15]. Due to control of the strengthening LPSO-phase composition, its orientation, size and volume distribution, the ultimate strength of Mg-RE alloys in the order of 600 MPa can be achieved, which is comparable with structural steel characteristics; the plasticity of ~30% and more is achieved, and also their ignition temperature (flame resistance) could be raised significantly [10, 14]. Yet, low corrosion resistance issue remains unresolved [16].

Mg is an electrochemically active metal with a low standard electrode potential of -2.37 V [17, 18]. Potential difference between the matrix (α-Mg) and the LPSO-phase can reach ~60–250 mV, which further lowers the alloy corrosion resistance due to the occurrence of micro-galvanic couples [5, 16, 19, 20]. Therefore, for Mg–RE (LPSO)-alloys to be implemented in unit and aggregate designs, additional solutions that neutralize this effect should be provided, for example, the application of protective coatings. Formation of multifunctional oxide ceramic layers on the alloy surface by plasma-electrolytic oxidation (PEO) appears most attractive technology [21, 22].

The PEO method is actively used for valve metals (Mg, Al, Ti, Zr) and is based on the oxidation of metals under high-energy electrical action in electrolyte solutions of various compositions [23–25]. The PEO method advantages are high adhesion of the oxide layer, single-stage treatment, relatively low cost, ease of layer application control and the environmental friendliness. Primary surface passivation occurs at the initial treatment stage, and, when certain critical voltage is reached, the dielectric «barrier» layer is broken down and plasma electric micro-arc discharges are formed across the treated surface [26]. Intense mass transfer due to high electric field strength and temperature gradients, combined with solution thermolysis, allows electrolyte components to be embedded into the oxide layers. The necessary oxide layer properties can be achieved by regulating the oxidation mode (the process electrical parameters), main components of the electrolyte and post-treatment processes [27, 28]. Such treatment makes it possible to obtain composite ceramic layers with the highest protective characteristics.

Despite plenty of studies on PEO of Mg alloys, we are aware of only 2 works in which this technology was applied to Mg alloys with LPSO-phase [11, 20]. However, the combined effect of electrolyte composition and technological process mode was not investigated in those studies.

PEO in combination with sealing post-treatment in a Ce-containing solution was used in paper [20] to increase the corrosion resistance of Mg–Y–Zn alloy with LPSO-phase. PEO was carried out in an alkaline-silicate-fluoride electrolyte at a forming pulse frequency of 500 Hz in the potentiostatic mode at a maximum initial current density of 400 mA·cm^{-2}. PEO allowed reducing the i_{corr} of the alloy by ~1.5 orders of magnitude. Subsequent holding in Ce-containing electrolyte made it possible to significantly reduce the surface porosity and the corrosion current to $2.0 \cdot 10^{-9}$ A·cm^{-2}.

The effect of the electrolyte composition on the oxidability of the Mg–Gd–Y–Zn alloy with LPSO-phase and the properties of oxide layers formed was investigated in [11]. The basic electrolyte components were sodium hydroxide and sodium fluoride, to which aluminate, phosphate and sodium silicate were added one at a time; the component combinations were also varied, and the effect of electrolyte composition on the anticorrosive properties of oxide layers was evaluated. The authors [11] found that the oxide layer formed in the electrolyte containing all these components at a concentration of 4 g·L^{-1} has the best anticorrosive properties – when tested in 3.5 wt.% NaCl, the authors managed to reduce the i_{corr} of the alloy by almost 3 orders of magnitude and increase the resistance of the barrier layer by more than 3 orders of magnitude compared to the resistance of charge transfer through the natural oxide film on the Mg(LPSO)-alloy. Among mono-additives, sodium silicate had the greatest effect on anticorrosive properties of the oxide layers, while the best combination of two additives was shown to be the sodium aluminate and sodium phosphate.

Along with the composition of electrolyte, the PEO technological mode has an important effect on increasing the anticorrosion and mechanical properties of the oxide layers [3, 26, 29–32]. In particular, an increase in the current frequency from 50 to 400 Hz during PEO demonstrated a greater effect on the anticorrosive performance than the use of preliminary anodic passivation [29]. The oxide layers obtained at a relatively high frequency (800 Hz) had smaller pore size and were much denser than the coatings obtained at 100 Hz [30]. However, the authors of [31] came to the opposite conclusion when studying the PEO of the AM50 magnesium alloy in the alkaline-phosphate electrolyte at three frequencies (10, 100 and 1000 Hz). They found that low-frequency PEO promotes sintering of the coating, making it denser and improving corrosion resistance. Thus, there is no consensus on the PEO frequency effect on the properties of the oxide layers formed. However, most authors believe that the intensity of the spark discharge is the most critical factor affecting the quality of coatings [33].

This work is aimed to study the combined effect of PEO electrolyte component composition and frequency of forming current pulses on the structure, mechanical and anticorrosive properties of oxide layers formed on the LPSO-phase magnesium alloy of the Mg-6.7Y–2.3Zn–1.1Zr (wt.%) system.

2. Materials and Methods

Oxide layers were obtained on the cast and heat treated $Mg_{97}Y_2Zn_1$ magnesium alloy with a strengthening LPSO-phase (SOMZ, Solikamsk, Russia). Chemical composition of the alloy (wt.%) was determined on the Thermo Fisher Scientific ARL 4460 OES optical emission spectrometer: 6.68 Y; 2.27 Zn; 1.07 Zr; 0.056 Nd; Mn < 0.005; Al, Fe < 0.002; Si, Ni, Cu < 0.001, the rest is Mg. The following phases were detected in the alloy: α-Mg, $Mg_{12}YZn$ (LPSO-phase) and $Mg_3Zn_3Y_2$ (W-phase) [34]. Before PEO, the samples were subjected to heat treatment according to the T61 mode: homogenizing annealing at a temperature of 525±5 °C, 24 hours, quenching in water heated to T >80 °C and aging at 200±5 °C, 100 hours. Such mode of heat treatment allows obtaining the maximum mechanical properties of this alloy.

Specimens for PEO were cut in the form of rectangular bars with dimensions (60×20×6) mm³, which were sanded before processing using SiC-based sanding paper with abrasive 600–1200–2500–5000 grit and isopropyl alcohol as a cutting compound.

PEO was carried out with alternating current from an original power source for 10 minutes at a constant current density of 10.0±0.5 A·dm⁻², the ratio of cathode and anode operating currents of half-cycles K/A = 0.50±0.02 and the electrolyte temperature of 286±2 K. Pulse-duty factor was 50%, the proportion of anode/cathode pulses in the total pulse duration was 50%/50% with a symmetrical pause between half–cycles. The frequency of trapezoidal forming pulses (50 Hz and 500 Hz) and the main electrolyte component, $NaAlO_2$ or Na_2SiO_3 (15 g·L⁻¹), which was added to the aqueous solution of KOH (1 g·L⁻¹), $Na_2HPO_4 \cdot 12H_2O$ (10 g·L⁻¹) and NaF (10 g·L⁻¹) were varied. The specimens obtained in the electrolyte with addition of sodium aluminate will be hereinafter referred to as PEO-A-50/500, and those with addition of sodium metasilicate – PEO-S-50/500.

Structural investigations of oxide layers were carried out on transverse metallographic sections using Carl Zeiss Sigma autoemission scanning electron microscope (SEM) with thermionic Schottky cathode (Germany) in the backscattered electrons (BSE) mode. Elemental (chemical) composition of oxide layers was studied integrally from the surface ($S \approx 160$ mm²) by X-ray fluorescence energy dispersive analysis (XRF) using the Shimadzu EDX-8000 energy dispersive X-ray fluorescence spectrometer (Rh-anode tube, U = 15–50 kV, I = 30–310 μA) and on transverse sections by energy dispersive X-ray microanalysis (EDXMA) using an X-ray spectral microanalysis unit based on the EDAX TEAM EDS energy spectrometer (SDD based EDAX "Apollo X" analyzer) of Sigma SEM. To remove polarization artifacts during SEM investigations, a thin conductive platinum layer was applied to the specimens by the "cold" magnetron (ion) sputtering method. The thickness T, μm and porosity P, % of oxide layers were evaluated from three panoramic cross-sectional images (≈500 μm long) using ImageJ software.

X-ray diffraction analysis of oxide layers was performed on the Shimadzu Maxima XRD–7000S diffractometer (Cu Kα radiation, X–ray tube with a long fine focus – LFF, Bragg-Brentano geometry) at a tube current of 40 mA, a voltage of 40 kV, a scanning speed of 0.25° min⁻¹ in the range of angles of 15–85° by 2θ in increments of 0.01°. The crystalline phases were identified using the Shimadzu PDF2 database. The quantitative phase composition of oxide layers was calculated by the Rietveld method. The proportion of X-ray amorphous phase in the oxide layer was also evaluated.

Hardness measurements according to Vickers $HV_{0.01}$ were performed on transverse specimens on the Shimadzu DUH-211S dynamic microhardness meter in accordance with ISO 14577-1:2015 recommendations under load of 98.1 mN (10 g) at least 10 times for each specimen.

The adhesive strength of oxide layers was measured using the Nanovea P-Macro scratch tester according to the linearly increasing load scheme as per the recommendations of ASTM C1624-05: a conical Rockwell indenter with a vertex angle of 120° and a radius at the apex of 100 nm was used; the scratch length – 15 mm; initial touch load – 0.1 N; final load – 30 N; indenter movement speed – 10 mm/min. At least 5 tests were performed on each specimen. After the scratches were applied, their panoramic shooting was carried out at x20 magnification using the Nanovea Stiks software, and the coordinate of oxide layer L_C massive fracture (tear) initiation was determined. Specific critical load of layer failure (F_C, N·μm⁻¹) was calculated from the relation of the oxide layer tearing load F to its thickness.

Electrochemical tests were carried out by methods of potentiodynamic polarization and impedance spectroscopy using the Elins P-45X potentiostat-galvanostat with an electrochemical impedance measurement module FRA-24M (Electrochemical Instruments) in 3.5 wt.% NaCl solution at room temperature (295±2 K). The tests were carried out in a three-electrode electrochemical hold-down cell CS936 (CorrTest, China) with a contact area of 1 cm². Platinum mesh (20×20 mm²) was used as an auxiliary electrode, and silver chloride electrode (Ag/AgCl) filled with saturated solution of potassium chloride was used as a reference electrode.

Electrode potential of no-polarization specimens (OCP) was stabilized for 60 minutes. Specimen potentiodynamic polarization (PDP) was carried out in the range from –150 mV to +1000 mV relative to OCP with a potential sweep rate of 1 mV/s. Polarization resistance R_P was determined based on ASTM G102-89(2015)e1 recommendations using the Stern-Geary constant according to the formula [35]:

$$R_P = \frac{\beta_a \beta_c}{2.303 i_{corr}(\beta_a + \beta_c)}, \qquad (1)$$

where β_a is the slope of the anode process Tafel curve, V/dec, and β_c is the slope of the cathode process Tafel curve, V/dec.

An important factor affecting the corrosion rate of the substrate is the effective interconnected porosity of oxide layers, which was evaluated by the electrochemical method according to the equation [21]:

$$P_{\text{eff}} = \left(\frac{R_{\text{Pb}}}{R_{\text{P}}}\right) \cdot 10^{-\left|\frac{\Delta E_{\text{corr}}}{\beta_{ab}}\right|} \qquad (2)$$

where P_{eff} is the dimensionless value showing the electrochemical porosity of the oxide layer, R_{Pb} and β_{ab} are the polarization resistance and the anode Tafelian slope of the bare alloy (substrate) with no oxide layer, R_{P} is the polarization resistance of the specimen with oxide layer, ΔE_{corr} is the difference in the corrosion potential between uncoated and coated specimens.

The investigation by electrochemical impedance spectroscopy (EIS) was carried out at a sinusoidal dither signal with 10 mV amplitude. The tests were run at electrode potential stabilized value in the frequency range from 10 mHz to 300 kHz. The analysis of experimental data and the calculation of equivalent circuit parameters were performed using the ZView software (Scribner Associates, USA).

The manufactured specimens were held for 14 days in a corrosive environment – 3.5 wt.% NaCl at 295±2 K. During this time, a periodic renewal of the corrosive medium was provided to maintain value pH = 7±0.5. Following the tests, the external control of the oxide layer state was carried out and the areas of corrosion damage were assessed.

3. Results

3.1. Voltage-time curves during PEO

Figure 1 shows the characteristic voltage-time curves during PEO in both electrolytes at 50 and 500 Hz current frequencies. The fast increase of the formation voltage observed in the first 60–70 seconds corresponds to the anodic passivation of the metal substrate. After initial time ~80 sec of the PEO process and under voltages about 230–250 V, the visual sparking on the alloy surface in the electrolyte starts, and then the brightness of the sparks and their number on the surface increase. In addition, the sparks on the anode in the silicate electrolyte seemed to be brighter and pointier, which indicates their greater power compared to the sparks during PEO in the aluminate electrolyte. As can be seen, the formation voltages in the silicate

electrolyte are higher than those in the aluminate electrolyte for both PEO frequencies, and the difference between them during the entire process of sparking is about 6–7%. It should be noted that the amplitude values of the anodic voltage increase with the increase in the frequency of the forming pulses from 50 Hz to 500 Hz for both electrolytes. A similar effect was observed by Kaseem et al. [36].

3.2. Structure, thickness and porosity of oxide layers

Figure 2 shows panoramic images of the oxide layers formed. The thickness of the oxide layers is approximately 40–50 μm and is virtually in dependent on the variable PEO parameters. The oxide layers formed at a pulse frequency of 50 Hz in both electrolytes have a very defective structure – there are delaminations and large (up to 10–15 μm) pores, transverse and main cracks, as well as local oxide layer discontinuities (Figure 2).

Increasing the forming pulse frequency to 500 Hz results in lower thickness heterogeneity and defectiveness (porosity, fracturing) of the layer; at the same time, there are no "uncoated" alloy zones or voids in the oxide layers, especially at the point where the LPSO-phase breaks the surface. The oxide layers formed in the electrolyte with sodium metasilicate addition have a pronounced two-layer structure.
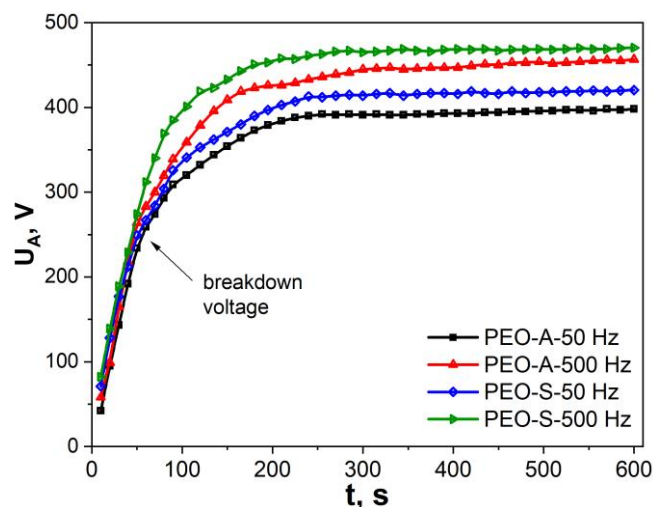

Figure 1 Voltage-time characteristic curves during PEO of the $Mg_{97}Y_2Zn_1$ alloy in the aluminate and silicate electrolytes at 50 and 500 Hz current frequencies.
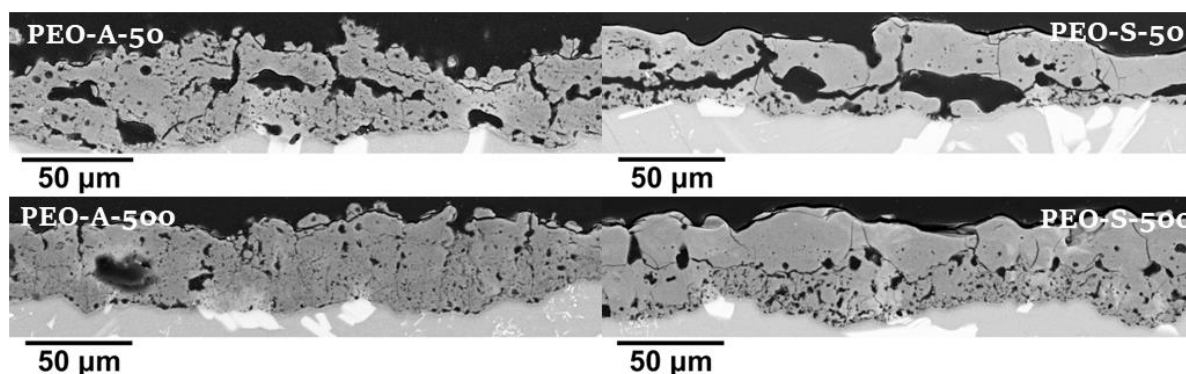

Figure 2 Transverse structure of the investigated oxide layers (SEM, BSE).

The main and largest defects are located in the inner zone of the oxide layers, directly at the substrate. The transverse structure of the PEO-S-50 specimen is characterized by high defectiveness, porosity (more than 13%), presence of multiple discontinuities and delaminations of the oxide layer. The use of sodium aluminate as an electrolyte component in combination with increased frequency during PEO allowed obtaining the most homogeneous and low-defect layer among the specimens under consideration.

Table 1 lists the average thicknesses of the investigated oxide layers and their internal porosity based on the results of SEM image processing. As can be seen from Table 1, the oxide layers obtained in the electrolyte with sodium aluminate have lower thickness and microhardness, but, at the same time, they are characterized by the least porosity, a smaller spread in the hardness values and the best adhesive strength.

3.3. Chemical (elemental) and phase composition of oxide layers

The main oxide layer elements are Mg, O, P, F, as well as Al or Si, depending on the electrolyte. These elements make up $\approx$90–96 wt.% of the oxide layer. Na, K and Ca, which are introduced into the oxide layer from the electrolyte, and alloy elements (Zn, Zr, Fe, Cu and Y) with a total content of 1.5–4.0 wt.% were also found.

According to the EDXMA data, higher concentrations of O, P and F and lower contents of Al and Si were obtained, since this analysis was made across the entire cross-section of the oxide layer, and not from its surface (Table 2).

Distribution of magnesium, oxygen and phosphorus for all oxide layers is equal and uniform (Figure 3).

For the layers obtained at industrial frequency (50 Hz), the highest concentration of the element introduced from the main electrolyte component (Al or Si) is observed in the surface layer. An increase in the pulse frequency during PEO results in a drop in the content of this element in the layer, but its distribution becomes more uniform. It should be noted that $NaAlO_2$ is more actively involved in the oxide layer formation. The Al content in the oxide layers under equal technological conditions is $\approx$22–23 wt.%, which is $\approx$ 2–3 times higher than the Si content.

There are differences in the content and distribution of fluorine in the oxide layers: its highest content and the most uniform distribution are characteristic of specimen PEO-S-500. For the other specimens, there is a predominant concentration of fluorine in a thin barrier layer at the alloy interface.

Figure 4 demonstrates XRD patterns of the $Mg_{97}Y_2Zn_1$ alloy and the investigated oxide layers, showing that the main phase in all specimens except PEO-S-50 is magnesium oxide (MgO, periclase, Fm3m), which is formed during the substrate oxidation assisted by micro-arc discharges in the process of PEO. The Mg_2PO_4F phase (wagnerite phosphoric acid mineral, monoclinic syngony) is also formed in the PEO-A-50 oxide layer. For PEO-S-50 specimen, the main phase is magnesium silicate, which is the product of interaction of molten magnesium metal and magnesium oxide with silicate ions from the electrolyte. In PEO-S-500 specimen, magnesium oxide becomes the main phase again (Table 3).

The second phase in the oxide layer by weight percentage is determined by the dominant electrolyte component: magnesium aluminate phase $MgAl_2O_4$ (cubic syngony, Fd-3m) is formed in the oxide layer in the aluminate electrolyte, and magnesium silicate Mg_2SiO_4 (forsterite, orthorhombic syngony, Pmnb) is formed in the silicate electrolyte. There is also some layer amorphization, as evidenced by amorphous halo in the region of 30–45 degrees along 2θ for PEO-A specimens, and in the region of 25–40 degrees for PEO-S series specimens.

Calculation of the degree of oxide layers crystallinity (Table 3) showed that the amorphous phase content in the oxide layers obtained in the aluminate and silicate electrolytes at industrial frequency is $\approx$18 and 13.6 vol.%, respectively.

Table 1 Characteristics of oxide layers produced.

Specimen	T (μm)	P (%)	$HV_{0.01}$ (MPa)	F_C (N·μm^{-1})
PEO-A-50	41.4±6.1	9.9±0.7	686±138	0.60±0.11
PEO-A-500	43.6±9.4	5.9±0.6	661±76	0.67±0.14
PEO-S-50	48.6±12.3	13.1±1.0	716±219	0.36±0.09
PEO-S-500	46.0±10.1	9.2±2.7	535±171	0.44±0.10

* Table 1 shows ±2σ as errors; T is the thickness, μm; P is the porosity, %; $HV_{0.01}$ is the microhardness, MPa; F_C is the specific critical tearing load, N·μm^{-1} of oxide layers.

Table 2 Chemical (elemental) composition of oxide layers.

Specimen	Method	Element content (wt.%)					
		Mg	O	Al	Si	P	F
PEO-A-50	XRF	34.82±0.08	23.10±0.30	22.63±0.06	–	4.16±0.01	2.33±0.16
	EDXMA	31.52±0.67	30.60±0.71	17.69±1.43	–	12.47±0.36	7.71±1.50
PEO-A-500	XRF	38.10±0.08	23.09±0.28	22.08±0.05	–	4.68±0.02	2.89±0.15
	EDXMA	33.27±1.41	30.46±0.76	15.59±0.89	–	12.13±0.65	8.57±1.22
PEO-S-50	XRF	43.73±0.09	25.70±0.33	–	12.32±0.01	5.03±0.01	3.50±0.19
	EDXMA	35.78±1.05	31.12±0.93	–	12.02±1.29	11.67±0.30	9.42±1.33
PEO-S-500	XRF	48.64±0.10	21.77±0.27	–	6.82±0.02	4.70±0.01	8.68±0.13
	EDXMA	37.66±0.76	28.04±0.60	–	9.25±0.41	11.68±0.38	13.38±0.56

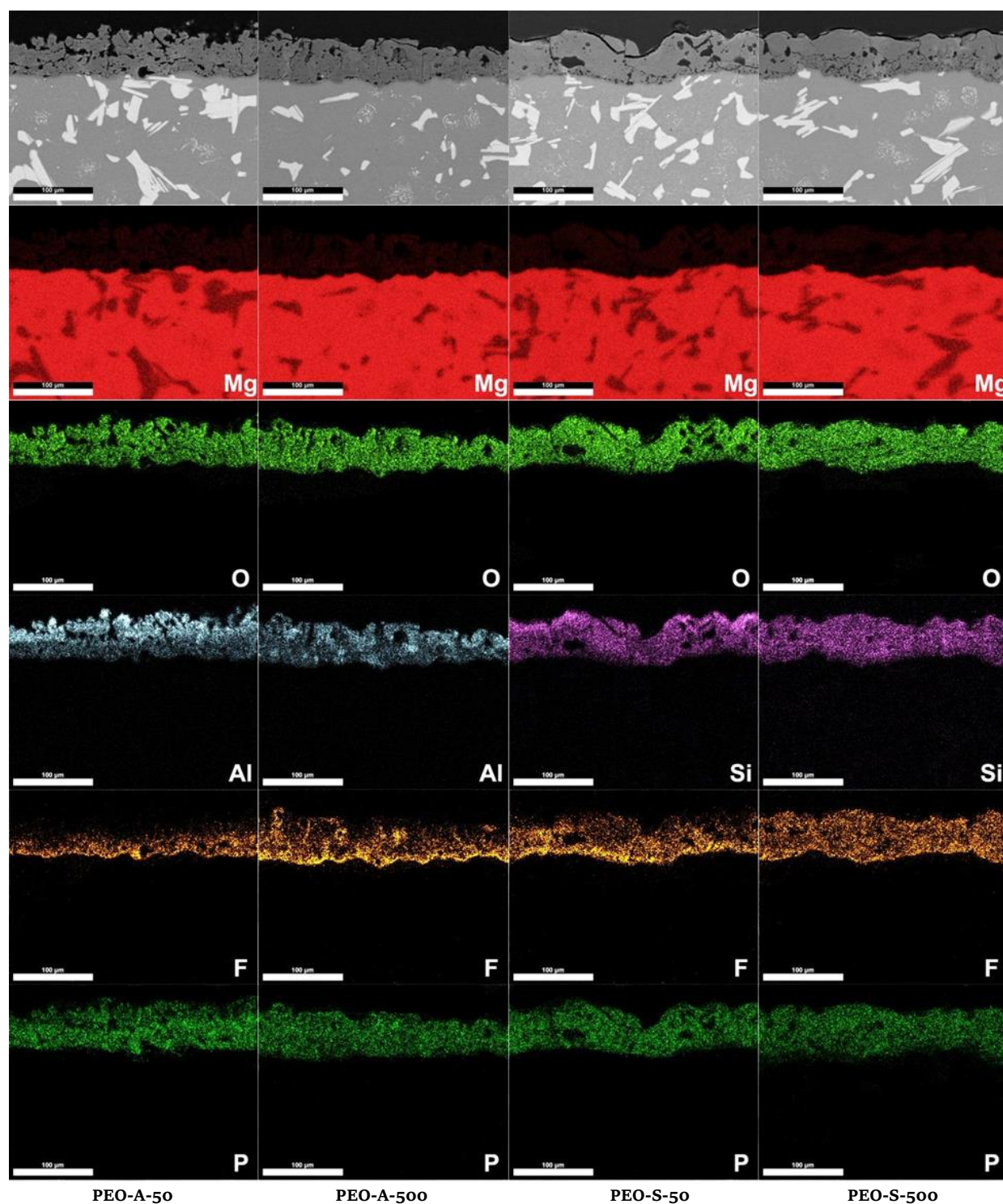* ± 3σ is listed as error in measurement.

Figure 3 The BSE micrographs of the oxide layer (top row) and the distribution maps of the main elements in it (Mg, O, Al or Si, F and P).

Table 3 Quantitative phase composition of oxide layers.

Specimen	Phase content in the oxide layer				Amorphous phase (vol.%)
	MgO	MgAl$_2$O$_4$	Mg$_2$SiO$_4$	Mg$_2$PO$_4$F	
PEO-A-50	46.6	40.3	–	13.1	17.94
PEO-A-500	69.4	30.6	–	–	27.32
PEO-S-50	15.4	–	84.6	–	13.57
PEO-S-500	92.4	–	7.6	–	37.35

* The degree of reliability of R^2 approximation of model empirical diffractogram in Jana 2006 software from profile analysis by the Rietveld method with account for the statistical weight of each point (wR_p) is 95–96% for all specimen.

An increase in the frequency of forming pulses to 500 Hz results in a higher content of the amorphous phase in the oxide layer composition, which is especially evident for the PEO-S-500 specimen – the amorphous phase proportion increased by 2.8 times.

Also, the composition of X–ray amorphous phase probably includes phosphorus crystalline nuclei and fluorine-containing phases, since crystalline phases containing P and F were detected only for the PEO-A-50 specimen, and the elemental analysis showed total content of these elements in the oxide layer ≈7–13 wt.% (Table 2).
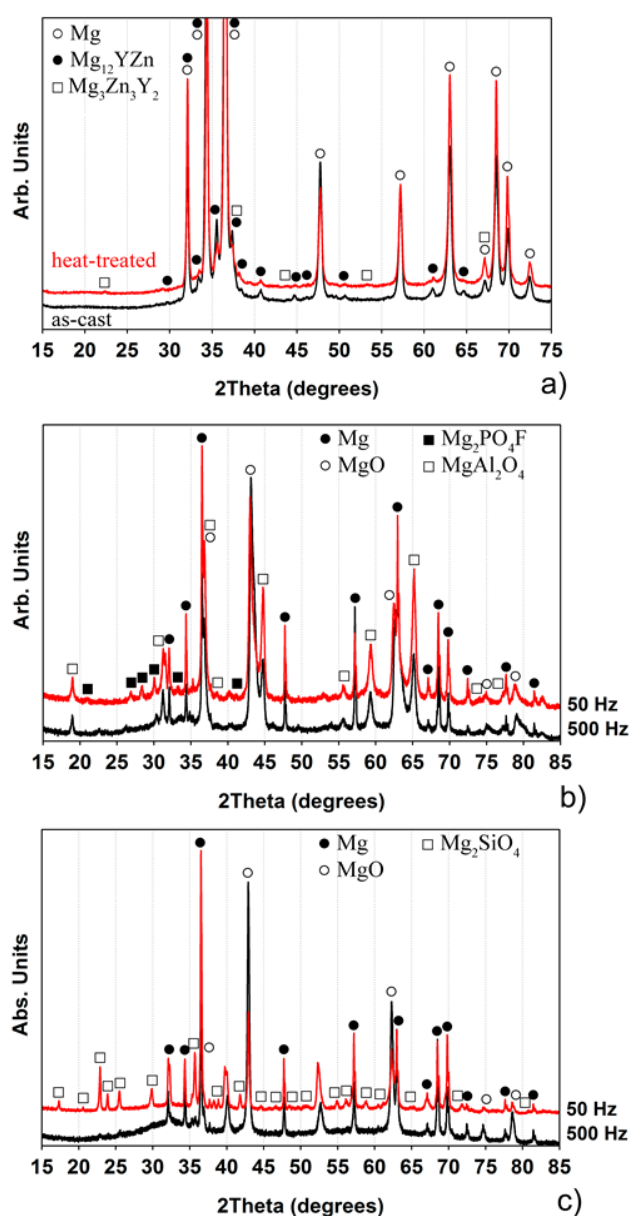
Figure 4 XRD patterns of the $Mg_{97}Y_2Zn_1$ alloy (as cast and heat treated before PEO) (a) and oxide layers obtained in aluminate (PEO-A) (b) and silicate (PEO-S) (c) electrolyte at forming pulse frequencies of 50 and 500 Hz.

For the oxide layers formed in the aluminate electrolyte, the magnesium oxide content increases with an increase in the pulse frequency of the forming current by about 1.5 times (to ≈69.4 wt.%), and the fraction of the second phase ($MgAl_2O_4$) drops by ≈30% (to 30.6 wt.%).

When silicate electrolyte is used, a significant activation of substrate oxidation is noted with increasing frequency of PEO pulses from 50 to 500 Hz: the MgO phase content increases by 6 times (to 92.4 wt.%) and the forsterite content drops by ≈11 times (to ≈7.6 wt.%).

3.4. Hardness and adhesive strength

The oxide layers obtained in PEO at industrial frequency have the highest average microhardness (≈690–720 MPa) (Table 1). Simultaneously, they are characterized by the greatest heterogeneity and porosity – HV variation coefficients reach 30%. With an increase in the forming pulse

operating frequencies there is a certain decrease in hardness, which, however, is not critical, given the spread in measurement statistics. The PEO-A-500 specimen, with a slight decrease in hardness (less than 4%), is characterized by its greater uniformity – 661±76 MPa.

Figure 5 presents the traces of oxide layer scratches, for which the fracture coordinate (L_C) is as close as possible to the average value. All specimens are characterized by occurrence of obvious destruction of the oxide layer and exposure of the substrate. The average indenter travel to the substrate exposure for the oxide layer samples formed in the aluminate electrolyte is ≈35% higher than the coordinate L_C of the specimens of the PEO-S series. A visible effect of using higher frequencies in PEO is also noteworthy – the tearing load L_C increased by ≈20–25%, depending on the composition of the electrolyte. For the PEO-A-500 specimen, the best adhesive strength was recorded in 2 out of 5 tests, no massive fracture of the oxide layer with entire substrate exposure occurred, and other scratches are characterized by the average travel L_C ≈ 14.3 mm with a total path length of 15 mm until the metal was completely exposed.

Similar trends persist when proceeding to specific indicators of adhesive strength assuming different thickness of specimens (Table 1): the PEO-A-500 specimen has maximum average value F_C ≈ 0.67 N/μm. Thus, the best oxide layer adhesion-cohesive characteristics are achieved by using the electrolyte with addition of sodium aluminate at a forming pulse frequency of 500 Hz.

It should be noted that an increase in the adhesive strength of oxide layers is accompanied by a drop in their hardness (Table 1), which suggests the mechanism of layer brittle fracture in scratch testing.

3.5. Corrosion resistance

Figure 6 shows the Tafel curves of the investigated specimens in a corrosive environment of 3.5% (wt.) NaCl. The formation of a protective ceramic layer on the specimens' surface allowed reducing the corrosion current density of $Mg_{97}Y_2Zn_1$ alloy by 1 to 3 orders of magnitude (Table 4). The least effect is achieved with PEO at industrial current frequency: for specimens obtained at a frequency of 50 Hz in the electrolyte with addition of $NaAlO_2$ and Na_2SiO_3, slowdown of the alloy corrosion rate (drop in the corrosion current i_{corr} density) was ≈11 and ≈19 times, respectively. Despite the lower i_{corr} value of the PEO-S-50 specimen, its polarization resistance is lower than R_P of the PEO-A-50 specimen by about 7 times. With similar parameters of cathodic branches of hydrogen reduction for both specimens, anodic branch of the PEO-S-50 specimen has a steeper rise, which indicates a more rapid increase in the rate of Mg dissolution under anodic polarization.

The use of electrolyte with addition of sodium metasilicate in combination with the industrial frequency of forming pulses results in the formation of the most porous oxide layers according to PDP data (≈14%).
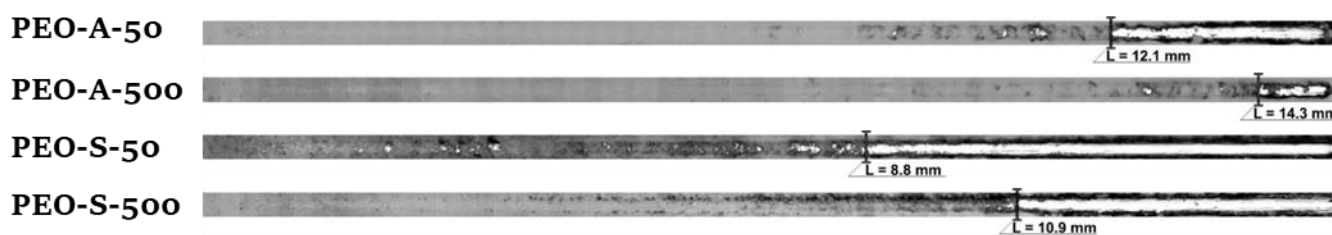
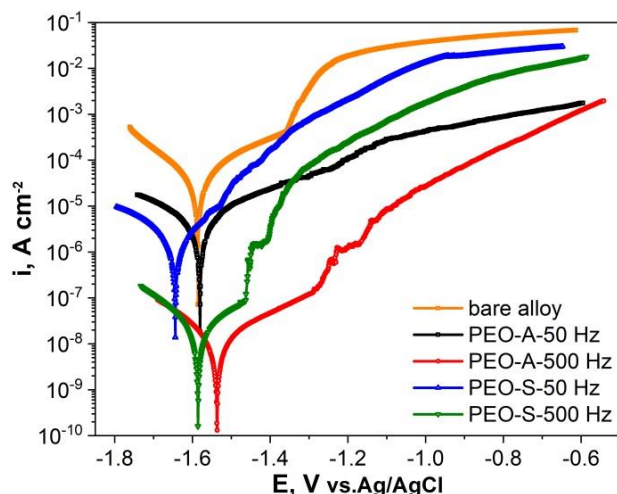**Figure 5** Images of scratches in the investigated oxide layers (x20, optical light microscopy).

Figure 6 Polarization (Tafel) curves of the initial (bare) $Mg_{97}Y_2Zn_1$ alloy and after PEO.

An increase in the current frequency to 500 Hz made it possible to further reduce i_{corr} of PEO-A-500 and PEO-S-500 specimens by more than 2 orders of magnitude – to ≈14 and 23 nA·cm⁻², respectively. The shift of E_{corr} of the PEO-A-500 specimen towards positive direction relative to other samples may be due to a decrease in the number of Cl⁻ adsorption centers because of the formation of densest PEO layer. A higher value $R_P ≈ 2.8$ MΩ·cm² should be noted in the specimen with the oxide layer obtained in aluminate electrolyte, for which the slope of anodic branch is more gentle. The PEO-S-500 specimen, despite the low i_{corr} value, is characterized by a "breakdown" of oxide layer under only a slight anode polarization (≈ +0.15 V) and a sharp increase in the current density (by more than an order of magnitude).

The results of potentiodynamic polarization are in good agreement with the impedance spectroscopy data. Figure 6 shows the results of alternating current (EIS) measurements of the investigated samples in Nyquist and Bode

coordinates. The impedance hodographs of the investigated samples are semicircles with different radii. PEO conducted at industrial current frequency allows increasing the charge transfer resistance of the surface layer by ≈7–10 times compared to the natural oxide film on the Mg-RE (LPSO) alloy (Figure 6, insets). An increase in the frequency of forming pulses to 500 Hz in both electrolytes results in a significant gain (by ≈2 orders of magnitude) in the radius of circle and scalar impedance, indicating high protective properties of such oxide layers.

Modeling using equivalent electrical circuits was carried out to detail the electrochemical processes at the alloy/electrolyte interface. The impedance spectrum of bare alloy was modeled using a simple equivalent diagram with a single R–C(CPE)-circuit (Figure 7), and it is limited to the high and medium frequency regions. The capacitive component depends on the capacitance of the double electric layer, and the resistance of charge transfer across the interface. For best description of experimental data, a constant phase element (CPE) was used instead of the ideal capacitance, taking into account the heterogeneity of the natural oxide film on the Mg alloy:

$$Z_{CPE} = \frac{1}{Q(j\omega)^n}, \qquad (3)$$

where Q is the frequency-independent parameter, j is the imaginary unit ($j = \sqrt{-1}$), ω is the cyclic frequency (ω=2πf), n is the exponential factor ($n ≤ 1$).

The spectra of samples with oxide layers have two characteristic "extrema" on the graph of the Bode diagram phase angle; therefore, a double loop R–C (CPE)-circuit was used for their detailing, to which two time constants correspond. Two inflections indicate a double zone coating structure; they are caused by the presence of an external porous PEO layer (CPE$_{out}$–R$_{out}$) and an internal dense barrier (CPE$_{in}$–R$_{in}$) layer.

Table 4 Results of PDP tests of $Mg_{97}Y_2Zn_1$ alloy in the initial state and after PEO, holding in a corrosive environment of 3.5 wt.% NaCl for 1 hour.

Specimen	OCP (V)	i_{corr} (µA·cm⁻²)	E_{corr} (V)	R_P (MΩ·cm²)	P_{eff} (%)
Bare alloy	−1.609±0.001	31.2±1.90	−1.582±0.006	(1.01±0.56)·10⁻³	–
PEO-A-50	−1.603±0.001	2.75±1.36	−1.544±0.077	0.083±0.034	3.42
PEO-A-500	−1.544±0.005	0.014±0.002	−1.541±0.013	2.757±0.603	0.11
PEO-S-50	−1.615±0.053	1.65±1.09	−1.585±0.062	0.012±0.008	13.9
PEO-S-500	−1.610±0.050	0.023±0.008	−1.610±0.050	1.411±0.389	0.07

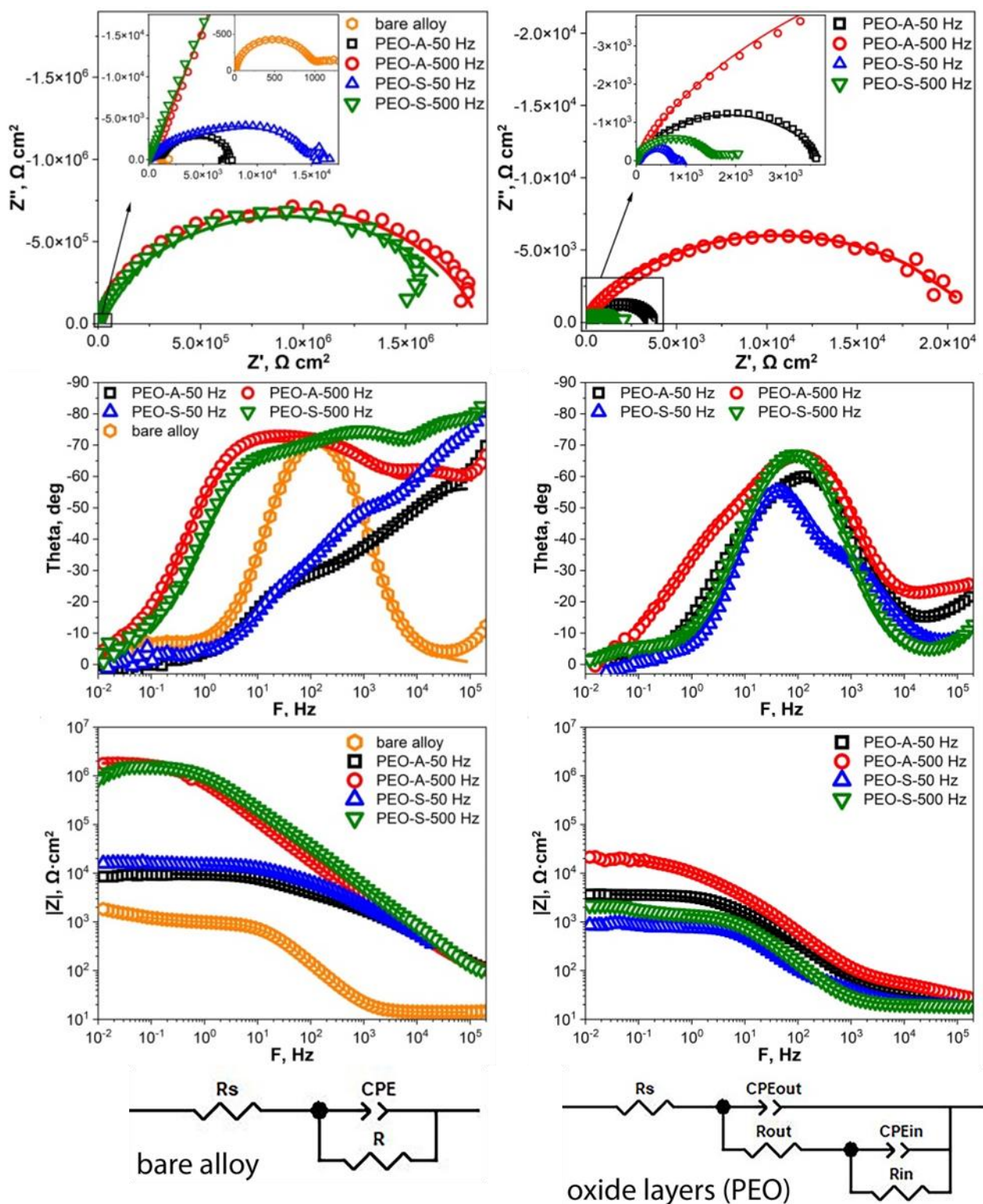* ±σ is given as the measurement error.

Figure 7 Nyquist and Bode curves of the initial $Mg_{97}Y_2Zn_1$ alloy and specimens with oxide layers after holding in corrosive environment: 1 hour (left) and 14 days (right) and equivalent circuits used to describe the EIS data. Markers are experimental points, lines are fitting.

The simulation results for the impedance spectra of specimens after 1 hour of holding in a corrosive environment are presented in Table 5. It is seen that the oxide layers formed during PEO in the silicate electrolyte have the greatest resistance of the coating outer part: R_{out} of the PEO-S-500 specimen is more than an order of magnitude higher than the values for the other specimens, which is in good agreement with its structure (Figure 1). Howev-

er, the main contribution to the anticorrosive properties of coatings is made by a thin barrier layer at the alloy interface [37, 38]. PEO at a frequency of 50 Hz results in an increase in the resistance of charge transfer across the alloy/electrolyte interface by about an order of magnitude (Table 5). Increasing the frequency of forming pulses from 50 Hz to 500 Hz during PEO further increases R_{in} by more than 2 orders of magnitude – to 1.5–2 $M\Omega\cdot cm^2$.

Table 5 Results of processing of EIS data for non-oxidized $Mg_{97}Y_2Zn_1$ alloy and alloy with oxide layer after 1 hour and 14 days of holding in corrosive environment.

Specimen	R_{out} (kΩ·cm²)	CPE$_{out}$		R_{in}^* (кΩ·cm²)	CPE$_{in}^*$		$|Z|_{f=0.01Hz}$ (kΩ·cm²)
		Q_{out} (Ω⁻¹·cm⁻²·cⁿ)	n_{out}		Q_{in} (Ω⁻¹·cm⁻²·cⁿ)	n_{in}	
1 hour of holding in 3.5% NaCl							
Bare alloy	–	–	–	0.9±0.3	$(1.6±0.1)·10^{-5}$	0.94±0.01	1.9±0.6
PEO-A-50	1.87±0.65	$(7.2±1.1)·10^{-7}$	0.70±0.01	6.3±2.1	$(2.5±1.8)·10^{-6}$	0.81±0.09	7.3±2.7
PEO-A-500	2.20±0.44	$(1.5±0.4)·10^{-7}$	0.83±0.02	$(2.1±0.7)·10^3$	$(7.6±1.7)·10^{-8}$	0.83±0.02	$(2.2±0.7)·10^3$
PEO-S-50	2.72±1.96	$(5.3±0.2)·10^{-7}$	0.74±0.01	9.1±4.0	$(2.4±0.3)·10^{-6}$	0.70±0.07	9.3±5.2
PEO-S-500	36.6±12.9	$(1.8±0.8)·10^{-8}$	0.81±0.03	$(1.5±0.2)·10^3$	$(8.7±4.7)·10^{-8}$	0.81±0.01	$(1.5±0.2)·10^3$
14 days of holding in 3.5% NaCl							
PEO-A-50	0.035±0.007	$(2.2±0.7)·10^{-5}$	0.55±0.03	4.3±1.2	$(8.4±3.1)·10^{-6}$	0.86±0.02	5.7±2.8
PEO-A-500	0.072±0.006	$(1.8±0.3)·10^{-5}$	0.58±0.02	13.4±7.1	$(2.6±0.6)·10^{-6}$	0.93±0.02	14.6±6.9
PEO-S-50	0.003±0.003	$(2.1±0.3)·10^{-5}$	0.80±0.13	0.6±0.2	$(4.2±4.2)·10^{-5}$	0.92±0.03	0.6±0.3
PEO-S-500	0.002±0.001	$(3.4±0.3)·10^{-5}$	0.65±0.03	1.3±0.5	$(2.8±1.3)·10^{-5}$	0.91±0.04	1.4±0.8

*CPE and R for the initial alloy are shown in columns R_{in} and CPE$_{in}$.

The frequency-independent parameter of the constant phase element (Q) corresponds to the interfacial capacitance, the value of which is inversely proportional to the thickness of the oxide layer (double electric layer) and is directly related to its surface area [23]. The specimens formed at 500 Hz have the least Q_{in} value. Thus, reducing the pulse duration triggers the formation of the densest barrier layer with fewer pores. The best anticorrosive characteristics were obtained for the PEO-A-500 specimen (Tables 4 and 5).

Holding of specimens in a corrosive environment for 14 days results in a sharp decrease in the scalar impedance values (Figure 7) and a change in phase shifts in the high and medium frequency regions. Thus, the outer zones of oxide layers almost cease to perform a protective function. The greatest degradation is demonstrated by specimens formed in the silicate electrolyte, which is also clearly seen in the surface images of specimens after corrosion tests (Figure 8). Two inflections of the phase angle of PEO-S-500 specimen in its initial state merge into one extremum during prolonged holding, and $|Z|_{f=0.01Hz}$ drops by more than 2.5 orders compared to the initial holding stage (1 hour) (Figure 6 and 7).

Specimens formed in the aluminate electrolyte display less tendency to degradation during prolonged holding. Despite the drop in the resistance of the outer part of the layer, R_{in} of the PEO-A-50 specimen decreased by less than 1.5 times (to ≈4.3 kΩ·cm²). The PEO-A-500 specimen shows highest values of scalar impedance after long holding. Despite R_{in} dropping to ≈13 kΩ·cm², the oxide layer continues to perform its protective function.

Before immersion, the surface of all specimens was homogeneous with no visible defects. After long exposure to corrosive environment, the specimens obtained in the electrolyte with addition of sodium metasilicate suffered general corrosion. The deepest corrosion pits are displayed by the PEO-S-50 specimen. The specimens formed in the aluminate electrolyte showed only a slight local corrosion on rectangular edges or near the side faces, which indicates their good corrosion resistance and confirms the PDP and EIS test data. The PEO-A-500 oxide layer is characterized by the best anticorrosive properties, according to the results of EIS data and surface images.

4. Discussion

As can be seen from the results obtained, the oxide layers formed in two electrolytes, at high and low forming current pulse frequencies, have different structures, chemical and phase composition, and also significantly differ in anticorrosive and mechanical characteristics, which is indicative of dissimilarity in the processes of oxidation, mass transfer and generation of reaction products during the oxide layer formation.

As can be seen in Figure 2, a number of pores are observed in the places where the LPSO-phase reaches the magnesium alloy–oxide layer interface for samples PEO-A-50 and PEO-S-50, and the integrity of the barrier layer is broken.
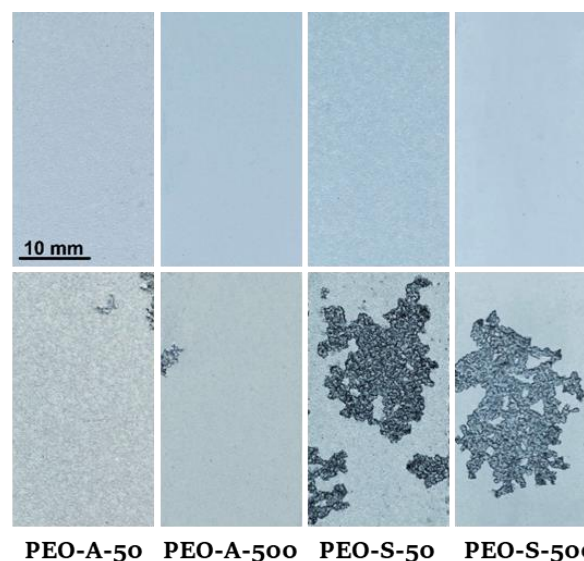

Figure 8 Macroscopic images (optical light microscopy) of specimens with oxide layers before (upper row) and after (lower row) immersion in 3.5 wt.% NaCl for 14 days.

This suggests that the LPSO phase has a negative effect on the process of ignition and combustion of a microarc discharge, and its effect is similar to the effect of silicon in silumins during PEO [39, 40]. At the same time, this effect is leveled by an increase in the frequency of forming pulses in both electrolytes, which indicates the possibility of controlling the process of PEO of magnesium alloys with an LPSO phase. The role of the LPSO phase in the formation of the fine structure of the oxide layer and, specifically, the barrier layer at the magnesium alloy–oxide layer interface will be the subject of our further research.

A substantial difference in the chemical (elemental) composition of the obtained oxide layers is noteworthy – with the same concentration of sodium aluminate or sodium metasilicate in the electrolyte, the amount of aluminum in the layer is about 1.5–3 times greater than that of silicon (based on two methods data). Apparently, this is due to the higher reaction rate of spinel formation $MgO + Al_2O_3 = MgAl_2O_4$ [41] compared with the reaction of magnesium silicate formation $MgO + SiO_2 = MgSiO_3$ [42].

It is also known that the molar mass of sodium silicate (122 g·mol^{-1}) is about 1.5 times greater than that of sodium aluminate (82 g·mol^{-1}). For each of these electrolyte components, the amount of substance and, consequently, the amount and concentration of aluminate or silicate ions that are present in the electrolyte and can potentially participate in the oxide layer formation during PEO can be calculated. For a mass concentration of 15 g·L^{-1} of each of the components, the molar concentrations of aluminate and sodium silicate in the electrolyte are 0.18 mol·L^{-1} and 0.12 mol·L^{-1}, respectively. With complete dissociation of substances into ions and with their molar concentrations factored in, $C[AlO_2^-]$ in the electrolyte will be 10.6 g·L^{-1}, while $C[SiO_3^{2-}] = 9.12$ g·L^{-1}. Thus, with an equal mass concentration of sodium aluminate or sodium silicate in the electrolyte, the concentration of aluminate ions capable of reacting during layer formation is about 16% greater than silicate ions, which can further increase the amount of aluminum in the layer compared to the amount of silicon.

The increase of the fluorine content in the oxide layers formed in the silicate electrolyte should be noted. It can be assumed that silicate ions accumulate around the anode and form around it a «silicate film» which hinders the microarc breakdown.

As a result, the forming voltages increase for the initiation of the microarc discharge (MAD) which leads to occurrence of the B-type discharges [43] that penetrate the whole thickness of the oxide layer and reach the interface between the substrate and the coating. In this case, a larger volume of molten metal is formed, and a stronger splash of it to the micropore channel occurs, which leads to a more active capture of the electrolyte components by the melt.

In addition, it can be seen that the highest content of Al is observed in the outer zone of the coating (Figure 3),

which indicates the incorporation of aluminum into the oxide layer by A and C discharges [43, 44].

It is worth noting that with an increase in the frequency of the forming current pulses, the proportion of aluminum or silicon in the oxide layer slightly decreases, while porosity and crystallinity of oxide layers are significantly reduced (Tables 1, 3 and 4, and Figure 2); at the same time, the achieved thickness of oxide layers is maintained (Table 1). Apparently, this is a consequence of significant differences in the characteristics of micro-arc discharges (MAD) that occur at different frequencies of forming pulses in the course of PEO.

It is well known that the formation of oxide layer is a cyclic electrochemical process; its three main stages are repeated throughout the treatment [45, 46] correspond to: 1) electrical breakdown of the barrier layer at the metal/oxide layer interface and formation of a vapor-gas phase in the discharge (micropore) channel; 2) micro-arc breakdown of the vapor-gas bubble and beginning of the rapid melting of the substrate material due to a very high temperature in the micro-arc [47, 48] accompanied by simultaneous oxidation of alloy elements and reactions with electrolyte components; 3) spew of melt and reaction products to the surface their its rapid cooling, followed by solidification and formation of crystallites of different compounds [49]. All this is accompanied by intense mass transfer and gas formation processes, which determine the composition and structure of the layer and depends mainly on the characteristics of MAD during PEO.

Duration of one MAD burning in the anode half-cycle ranges from several to tens of microseconds at the initial stages of the oxide layer formation to 100–200 µs when thicknesses in the region of 50–100 µm are reached. At the same time, the "incubation period" (pause between MAD occurrence) reaches several tens to hundreds of microseconds [46, 50]. With industrial PEO frequency of 50 Hz in a "symmetrical" anode-cathode cycle and a pulse-duty factor of 50%, the anode pulse duration is 5000 µs, which is 1–2 orders longer than the duration of MAD. As a result, several MAD "waves" and their cascades can occur in one anode pulse that have strong thermal effect and contribute to heating the sections of oxide layer adjacent to the MAD breakdown region. At PEO pulse frequency of 500 Hz, the experimental duration of anode pulse is 500 µs, which, nevertheless, is significantly longer than the burning time of individual MADs. It indicates that the microarc discharges at both frequencies belong to the same B-type, when the dielectric breakdown of oxide layer occurs through the vapor-gas bubble in the micropore channel up to the metal substrate, and the molten metal is ejected from the substrate into the micropore channel and onto the surface of the coating, where it rapidly oxidizes and solidifies [3, 51].

It can be assumed, however, that the main reason for the observed changes in the structure and phase composition of the oxide layers is not the reduced duration of

forming pulse itself, but a decrease in the power and duration of "life" (burning) of a single MAD at a shorter anode pulse, which results in a lesser thermal effect of a single MAD on the substrate.

Since the current density is kept constant during PEO, the number of MADs should increase proportionally with a decrease in their duration (or power) to ensure a given current value. At the same time, the total thermal effect does not change, but the maximum temperatures, reached in the substrate under a single MAD, fall. As demonstrated in paper [38], the volume of melting metal is approximately proportional to the duration of micro-arc burning; therefore, a decrease in the MAD duration with a proportional increase in their number will not affect the total volume of melted metal, i.e., it will not affect the thickness of oxide layer, which was observed in our experiments (Figure 2 and Table 1). However, a decrease in the maximum temperatures during melting of the substrate can trigger significant changes in the structure of the oxide layer being formed.

The decrease in the temperatures during formation of oxide layer at higher current pulse frequency is evidenced by a change in the phase composition – no Mg_2PO_4F phase, characteristic of the PEO-A-50 layer and formed as a result of high-temperature sintering, was detected in the PEO-A-500 oxide layer [53]. We assume that the probable mechanism of the Mg_2PO_4F (wagnerite) formation is the high-temperature sintering of MgF_2 and $Mg_3(PO_4)_3$ according to the reaction equation:

$$Mg_3(PO_4)_2 + MgF_2 \rightarrow 2Mg_2PO_4F. \qquad (4)$$
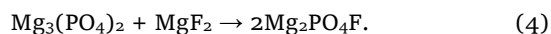
It is worth noting that the wagnerite phase was found only in the PEO-A-50 oxide layer and was not observed in other specimens in which phosphorus and fluorine are included only in the amorphous phase. The reasons for this phenomenon are not entirely clear, and it will be the subject of our further research.

A decrease in the maximum temperatures during melting should lead to a decrease in the melted volume under a single MAD, which increases the cooling rate during solidification. This, in turn, leads to an increase in the fraction of the amorphous phase in the layer, i.e., to a decrease in its crystallinity, which is observed experimentally (Table 3).

The overall reduction in the porosity and the size of individual pores in the structure of the oxide layer (Figure 1) is also likely the result of a decrease in the maximum temperatures reached. Shorter MAD "lifetime" (or smaller MAD power) results in a drop not only in the volume of melted substrate under a single MAD, but also in a reduced boiling of liquid metal (magnesium). It is the boiling of metal melt that is mainly responsible for pore formation: bubbles with metal vapor formed during boiling then turn into pores at rapid melt cooling and formation of metal oxide. A decrease in the temperature of molten substrate (magnesium) caused by lower MAD

duration or power, and, consequently, a decrease in the fraction of boiling and evaporating part of the melt results in a decrease in porosity caused by metal vapor bubbles. Furthermore, this leads to a decreased speed of movement of the melt inside the micropore channel during the spew and, consequently, to a less turbulent flow of liquid and capture of a lesser part of vapor-gas phase by the moving melt. Taken together, all this leads to the formation of a more homogeneous and less porous structure of oxide layer, with an increased fraction of amorphous phase.

It was found that the short-term corrosion resistance of oxide layers formed at 500 Hz is distinctly better than that of the one formed at 50 Hz (Tables 4 and 5). This is probably due to a decrease in porosity as well as compaction of the barrier layer (R_{in} increase by about 3 orders of magnitude – Table 5) due to less thermal cracking and gas formation during solidification. Pitting corrosion is known to be the main corrosion type in magnesium alloys in chloride-containing environments [54]. Consequently, micropores and pore channels of oxide layers negatively affect the corrosion characteristics. Larger pores and microcracks of the PEO-A-50 and PEO-S-50 specimens increase the actual area exposed to the corrosive solution, i.e., they contribute to the magnesium substrate contacting it, which leads to higher values of the corrosion current density (Table 4).

It can be argued that degradation of oxide layers in a corrosive environment is most affected by the composition of PEO electrolyte. In particular, the PEO-S-50 specimen with higher short-term anticorrosive characteristics (vs PEO-A–50) after 14 days of holding showed most extensive (more than 50% of the specimen area – Figure 8) and deep corrosion lesions. Similar trends were observed for oxide layers formed at 500 Hz. PEO-S-500 specimen demonstrates the highest degree of degradation relative to the initial state: $|Z|_{f=0.01Hz}$ decreases by 3 orders of magnitude – from 1.5 MΩ·cm² to 1.4 kΩ·cm² (Table 5). Probably, this fact is associated with the lack of a fluorine-enriched barrier layer (thickness <500–1000 nm, Figure 2, distribution F), which has a passivating effect on the surface of the magnesium substrate and gives the barrier layer higher anticorrosive properties [20, 55–57]. It is also likely that the high content of MgO in this oxide layer (92.4%), which tends to dissolve if contacting moisture for long, has an additional effect on the higher degree of degradation.

5. Limitations

The main problem appeared during this research is stabilization of the open circuit potential (OCP) of the samples. Due to the strong fluctuation of OCP on Mg-RE (LPSO) alloy with oxide layer formed by PEO, the exposure time in a corrosive environment before electrochemical measurements

and especially EIS tests had to be increased to 2 hours or more.

6. Conclusions

The effects of current pulse frequency and electrolyte composition during PEO of $Mg_{97}Y_2Zn_1$ magnesium alloy with strengthening LPSO-phase were studied. The PEO of the alloy under study at higher frequency of forming current pulses (500 Hz) enables forming higher-quality and more uniform oxide layer with enhanced hardness, adhesive strength and anticorrosive properties, the latter exceeding by more than 2 orders of magnitude the parameters obtained using the standard industrial frequency of 50 Hz. For both alkaline-phosphate-fluoride electrolytes used, with the addition of sodium aluminate or sodium silicate, at increased frequencies of forming pulses, a continuous oxide layer can be formed with no pronounced delaminations from the substrate or internal pores. The best results were obtained when using electrolyte with addition of sodium aluminate. The use of silicate electrolyte increases the porosity, especially at the frequency of 50 Hz. The use of aluminate electrolyte in combination with higher pulse frequency during PEO allows achieving the best long–duration corrosion resistance – an order of magnitude higher than when using silicate electrolyte, and also providing the highest and uniform hardness ($HV_{0.01}$ 650–700 MPa) and adhesive strength (0.7–0.8 N·µm^{-1}) of oxide layers on Mg-RE alloy with strengthening LPSO-phase. The revealed changes in the structure, composition and properties of oxide layers at the increase in the forming pulse frequency are associated with a drop in the maximum temperatures reached during MAD-assisted substrate melting and are probably due to a decrease in the burning duration and power of individual micro-arc discharges.

● Author contributions

Conceptualization: A.O.C., A.V.P., A.V.K, M.M.K.

Data curation: P.A.G., A.V.K., A.O.C., A.V.P.
Formal Analysis: A.O.C., P.A.G.
Funding acquisition: A.V.P.
Investigation: A.O.C., P.A.G., A.G.D., E.D.B., M.R.S., A.V.P.
Methodology: A.O.C., A.G.D., M.R.S., E.D.B., A.V.P., A.V.K., M.M.K.
Project administration: A.V.P.
Resources: A.V.P., M.M.K.
Supervision: M.M.K.
Validation: A.V.P., A.V.K., M.M.K.
Visualization: A.O.C., P.A.G., A.G.D., E.D.B., M.R.S., A.V.P.
Writing – original draft: A.O.C., P.A.G., A.G.D., E.D.B., M.R.S., A.V.P.
Writing – review & editing: A.O.C., A.V.P., A.V.K., M.M.K.

● Conflict of interest

The authors declare no conflict of interest.

● Additional information

Author IDs:
  Alisa O. Cheretaeva, Scopus ID 56100325600;
  Pavel A. Glukhov, Scopus ID 56556838300;
  Marat R. Shafeev, Scopus ID 56376647100;
  Alyona G. Denisova, Scopus ID 57008879600;
  Eugeny D. Borgardt, Scopus ID 57190491131;
  Anton V. Polunin, Scopus ID 57190496192;
  Alexander V. Katsman, Scopus ID 7004225554;
  Mikhail M. Krishtal, Scopus ID 14634063100.

Websites:
  Togliatti State University, https://www.tltsu.ru;
  Technion – Israel Institute of Technology, https://www.technion.ac.il/en/home-2.

References

1. Song J, She J, Chen D, Pan F. Latest research advances on magnesium and magnesium alloys worldwide. J Magnes Alloy. 2020;8:1–41. doi:10.1016/j.jma.2020.02.003

2. Yang C, Cai H, Cui S, Huang J, Zhu J, Wu ZZ, Ma Z, Fu RKY, Sheng L, Tian X, Chu PK, Wu ZZ. A zinc-doped coating prepared on the magnesium alloy by plasma electrolytic oxidation for corrosion protection. Surf Coatings Technol. 2022;433:128148. doi:10.1016/j.surfcoat.2022.128148

3. Liu X, Liu L, Dong S, Chen X-B, Dong J. Towards dense corrosion-resistant plasma electrolytic oxidation coating on Mg-Gd-Y-Zr alloy by using ultra-high frequency pulse current. Surf Coatings Technol. 2022;447:128881. doi:10.1016/j.surfcoat.2022.128881

4. Wang SD, Xu DK, Han EH, Dong C. Stress corrosion cracking susceptibility of a high strength Mg–7%Gd–5%Y–1%Nd–0.5%Zr alloy. J Magnes Alloy. 2014;2:335–341. doi:10.1016/J.JMA.2014.11.004

5. Li CQ, Xu DK, Zeng ZR, Wang BJ, Sheng LY, Chen XB., Han EH. Effect of volume fraction of LPSO phases on corrosion and mechanical properties of Mg–Zn–Y alloys. Mater Des. 2017;121:430–441. doi:10.1016/j.matdes.2017.02.078

6. Wang SD, Xu DK, Wang BJ, Sheng LY, Qiao YX, Han EH, Dong C. Influence of phase dissolution and hydrogen absorption on the stress corrosion cracking behavior of Mg–7%Gd–5%Y–

1%Nd–0.5%Zr alloy in 3.5 wt.% NaCl solution. Corros Sci. 2018;142:185–200. doi:10.1016/J.CORSCI.2018.07.019

7. Fattah-alhosseini A, Chaharmahali R, Babaei K, Nouri M, Keshavarz MK, Kaseem M. A review of effective strides in amelioration of the biocompatibility of PEO coatings on Mg alloys. J Magnes Alloy. 2022;10:2354–2383. doi:10.1016/j.jma.2022.09.002

8. Czerwinski F. Controlling the ignition and flammability of magnesium for aerospace applications. Corros Sci. 2014;86:1–16. doi:10.1016/J.CORSCI.2014.04.047

9. Xu D, Han EH, Xu Y. Effect of long-period stacking ordered phase on microstructure, mechanical property and corrosion resistance of Mg alloys: A review. Prog Nat Sci Mater Int. 2016;26:117–128. doi:10.1016/J.PNSC.2016.03.006

10. Qian Y, Zhao Y, Dong X, Yu W, Feng J, Yu H. Microstructure, Mechanical Properties and Fire Resistance of High Strength Mg-Gd-Y-Zr Alloys. Metals. 2022;12(9):1456. doi:10.3390/MET12091456

11. Wu J, Wu L, Yao W, Chen Y, Chen Y, Yuan Y, Wang J, Atrens A, Pan F. Effect of electrolyte systems on plasma electrolytic oxidation coatings characteristics on LPSO Mg-Gd-Y-Zn alloy. Surf Coatings Technol. 2023;454:129192. doi:10.1016/J.SURFCOAT.2022.129192

12. Wang G, Mao P, Wang Z, Zhou L, Wang F, Liu Z. High strain rates deformation behavior of an as-extruded Mg–2.5Zn–4Y magnesium alloy containing LPSO phase at high temperatures. J Mater Res. Technol. 2022;21:40–53. doi:10.1016/J.JMRT.2022.08.131

13. Volkova EF, Antipov VV, Zavodov AV. A Study of the Fine Structure and Phase Composition of Magnesium Alloy VMD16 in Cast and Homogenized Conditions. Met Sci Heat Treat. 2019;61:143–148. doi:10.1007/S11041-019-00390-6/METRICS

14. Dai J, Dong Q, Nie Y, Jia Y, Chu C, Zhang X. Insight into the role of Y addition in the microstructures, mechanical and corrosion properties of as-cast Mg-Gd-Y-Zn-Ca-Zr alloys. Mater Des. 2022;221:110980. doi:10.1016/J.MATDES.2022.110980

15. Dang C, Wang J, Wang J, Yu D, Zheng W, Xu C, Lu R. Effect of lamellar LPSO phase on mechanical properties and damping capacity in cast magnesium alloys. J Mater Res Technol. 2023;22:2589–2599. doi:10.1016/J.JMRT.2022.12.087

16. Wu L, Li Y, Cheng Y, Linghu F, Jiang F, Chen G, Teng J, Fu D, Zhang H. Microstructure evolution and corrosion resistance improvement of Mg–Gd–Y–Zn–Zr alloys via surface hydrogen treatment. Corros Sci. 2021;191:109746. doi:10.1016/J.CORSCI.2021.109746

17. Liu Y, Wen J, Li H, He J. Effects of extrusion parameters on the microstructure, corrosion resistance, and mechanical properties of biodegradable Mg–Zn–Gd–Y–Zr alloy. J Alloys Compd. 2022;891:161964. doi:10.1016/J.JALLCOM.2021.161964

18. Zhang W, Zhao MC, Wang Z, Tan L, Qi Y, Yin DF, et al. Enhanced initial biodegradation resistance of the biomedical Mg-Cu alloy by surface nanomodification. J Magnes Alloy. 2022. doi:10.1016/J.JMA.2021.12.013

19. Zhang J, Xu J, Cheng W, Chen C, Kang J. Corrosion Behavior of Mg-Zn-Y Alloy with Long-period Stacking Ordered Structures. J Mater Sci Technol. 2012;28:1157–1162. doi:10.1016/S1005-0302(12)60186-8

20. Mohedano M, Pérez P, Matykina E, Pillado B, Garcés G, Arrabal R. PEO coating with Ce-sealing for corrosion protection of LPSO Mg–Y–Zn alloy. Surf Coatings Technol. 2020;383:125253. doi:10.1016/j.surfcoat.2019.125253

21. Kaseem M, Fatimah S, Nashrah N, Ko YG. Recent progress in surface modification of metals coated by plasma electrolytic oxidation: Principle, structure, and performance. Prog Mater Sci. 2020;117:100735. doi:10.1016/j.pmatsci.2020.100735

22. Polunin AV, Cheretaeva AO, Borgardt ED, Shafeev MR, Katsman AV, Krishtal MM. Influence of nanoparticle additions to the electrolyte on the structure, composition and corrosion resistance of oxide layers formed by PEO on cast Mg alloy. J

Phys Conf Ser. 2020;1713:12036. doi:10.1088/1742-6596/1713/1/012036

23. Jangde A, Kumar S, Blawert C. Role of glycerine on formation & corrosion characteristic of PEO layer formed over Mg alloy in a high-concentrated mixed silicate-phosphate-based electrolyte. Surf Coatings Technol. 2022;450:128971. doi:10.1016/J.SURFCOAT.2022.128971

24. Yasui T, Hayashi K, Fukumoto M. Behaviors of Micro-Arcs, Bubbles, and Coating Growth during Plasma Electrolytic Oxidation of Titanium Alloy. Mater. 2023;16:360. doi:10.3390/MA16010360

25. Wu T, Blawert C, Lu X, Serdechnova M, Zheludkevich ML. Difference in formation of plasma electrolytic oxidation coatings on MgLi alloy in comparison with pure Mg. J Magnes Alloy. 2021;9:1725–1740. doi:10.1016/J.JMA.2021.03.017

26. Dehnavi V, Luan BL, Shoesmith DW, Liu XY, Rohani S. Effect of duty cycle and applied current frequency on plasma electrolytic oxidation (PEO) coating growth behavior. Surf Coatings Technol. 2013;226:100–107. doi:10.1016/j.surfcoat.2013.03.041

27. Kaseem M, Hussain T, Baek SH, Ko YG. Formation of stable coral reef-like structures via self-assembly of functionalized polyvinyl alcohol for superior corrosion performance of AZ31 Mg alloy. Mater Des. 2020;193. doi:10.1016/j.matdes.2020.108823

28. Fu W, Yang H, Li T, Sun J, Guo S, Fang D, et al. Enhancing corrosion resistance of ZK60 magnesium alloys via Ca microalloying: The impact of nanoscale precipitates. J Magnes Alloy. 2022. doi:10.1016/J.JMA.2022.06.011

29. Mohedano M, Lopez E, Mingo B, Moon S, Matykina E, Arrabal R. Energy consumption, wear and corrosion of PEO coatings on preanodized Al alloy: The influence of current and frequency. J Mater Res Technol. 2022;21:2061–2075. doi:10.1016/j.jmrt.2022.10.049

30. Lv GH, Chen H, Gu WC, Li L,Niu EW, Zhang XH, Yang SZ. Effects of current frequency on the structural characteristics and corrosion property of ceramic coatings formed on magnesium alloy by PEO technology. J Mater Process Technol. 2008;208:9–13. doi:10.1016/J.JMATPROTEC.2007.12.125

31. Srinivasan PB, Liang J, Balajeee RG, Blawert C, Störmer M, Dietzel W. Effect of pulse frequency on the microstructure, phase composition and corrosion performance of a phosphate-based plasma electrolytic oxidation coated AM50 magnesium alloy. Appl Surf Sci. 2010;256:3928–3935. doi:10.1016/J.APSUSC.2010.01.052

32. Li J, Bian Y, Tu X, Li W, Song D. Influence of surface roughness of substrate on corrosion behavior of MAO coated ZM5 Mg alloy. J Electroanal Chem. 2022;910:116206. doi:10.1016/J.JELECHEM.2022.116206

33. Zhu M, Song Y, Dong K, Shan D, Han EH. Correlation between the transient variation in positive/negative pulse voltages and the growth of PEO coating on 7075 aluminum alloy. Electrochim Acta. 2022;411:140056. doi:10.1016/J.ELECTACTA.2022.140056

34. Zhang Z, Liu X, Wang Z, Le Q, Hu W, Bao L, et al. Effects of phase composition and content on the microstructures and mechanical properties of high strength Mg–Y–Zn–Zr alloys. Mater Des. 2015;88:915–923. doi:10.1016/J.MATDES.2015.09.087

35. Hakimizad A, Raeissi K, Santamaria M, Asghari M. Effects of pulse current mode on plasma electrolytic oxidation of 7075 Al in Na_2WO_4 containing solution: From unipolar to soft-sparking regime. Electrochim Acta. 2018;284:618–629. doi:10.1016/j.electacta.2018.07.200

36. Kaseem M, Kamil MP, Ko YG. Electrochemical response of MoO2-Al2O3 oxide films via plasma electrolytic oxidation. Surf Coatings Technol. 2017;322:163–173. doi:10.1016/J.SURFCOAT.2017.05.051

37. Duan H, Yan C, Wang F. Effect of electrolyte additives on performance of plasma electrolytic oxidation films formed on magnesium alloy AZ91D. Electrochim Acta. 2007;52:3785–3793. doi:10.1016/j.electacta.2006.10.066

38. Ghasemi A, Raja VS, Blawert C, Dietzel W, Kainer KU. The role of anions in the formation and corrosion resistance of the plasma electrolytic oxidation coatings. Surf Coatings Technol. 2010;204:1469–1478. doi:10.1016/j.surfcoat.2009.09.069

39. Gulec AE, Gencer Y, Tarakci M. The characterization of oxide based ceramic coating synthesized on Al-Si binary alloys by microarc oxidation. Surf Coatings Technol. 2015;269:100–107. doi:10.1016/j.surfcoat.2014.12.031

40. Li K, Li W, Zhang G, Zhu W, Zheng F, Zhang D, et al. Effects of Si phase refinement on the plasma electrolytic oxidation of eutectic Al-Si alloy. J Alloys Compd. 2019;790:650–656. doi:10.1016/J.JALLCOM.2019.03.217

41. Saheb N, Lamara S, Sahnoune F, Hassan SF. Kinetic analysis of the formation of magnesium aluminate spinel ($MgAl_2O_4$) from α-Al_2O_3 and MgO nanopowders. J Therm Anal Calorim. 2022;147:11549–11559. doi:10.1007/S10973-022-11344-1/TABLES/5

42. Mikhail SA, King PE. High-temperature thermal analysis study of the reaction between magnesium oxide and silica. J Therm Anal. 1993;40:79–84. doi:10.1007/BF02546557/METRICS

43. Zehra T, Patil SA, Shrestha NK, Fattah-alhosseini A, Kaseem M. Anionic assisted incorporation of WO_3 nanoparticles for enhanced electrochemical properties of AZ31 Mg alloy coated via plasma electrolytic oxidation. J Alloys Compd. 2022;916:165445. doi:10.1016/J.JALLCOM.2022.165445

44. Toulabifard A, Rahmati M, Raeissi K, Hakimizad A, Santamaria M. The Effect of Electrolytic Solution Composition on the Structure, Corrosion, and Wear Resistance of PEO Coatings on AZ31 Magnesium Alloy. Coatings. 2020;10:937. doi:10.3390/COATINGS10100937

45. Yerokhin AL, Nie X, Leyland A, Matthews A, Dowey SJ. Plasma electrolysis for surface engineering. Surf Coatings Technol. 1999;122:73–93. doi:10.1016/S0257-8972(99)00441-7

46. Nominé AV, Troughton SC, Nominé AV, Henrion G, Clyne TW. High speed video evidence for localised discharge cascades during plasma electrolytic oxidation. Surf Coatings Technol. 2015;269:125–130. doi:10.1016/j.surfcoat.2015.01.043

47. Dunleavy CS, Golosnoy IO, Curran JA, Clyne TW. Characterisation of discharge events during plasma electrolytic oxida-

tion. Surf Coatings Technol. 2009;203:3410–3419. doi:10.1016/j.surfcoat.2009.05.004

48. Jovović J, Stojadinović S, Šišović NM, Konjević N. Spectroscopic study of plasma during electrolytic oxidation of magnesium- and aluminium-alloy. J Quant Spectrosc Radiat Transf. 2012;113:1928–1937. doi:10.1016/j.jqsrt.2012.06.008

49. Sundararajan G, Rama Krishna L. Mechanisms underlying the formation of thick alumina coatings through the MAO coating technology. Surf Coatings Technol. 2003;167:269–277. doi:10.1016/S0257-8972(02)00918-0

50. Troughton SC, Clyne TW. Cathodic discharges during high frequency plasma electrolytic oxidation. Surf Coatings Technol. 2018;352:591–599. doi:10.1016/j.surfcoat.2018.08.049

51. Hussein RO, Nie X, Northwood DO. An investigation of ceramic coating growth mechanisms in plasma electrolytic oxidation (PEO) processing. Electrochim Acta. 2013;112:111–119. doi:10.1016/J.ELECTACTA.2013.08.137

52. Pyachin SA, Burkov AA, Kaminskii OI, Zaikova ER. Melting of a Titanium Alloy Under the Action of Electrical Discharges of Different Duration. Russ Phys J. 2019;61:2236–2243. doi:10.1007/S11182-019-01661-8/METRICS

53. Ren L, Grew ES, Xiong M, Ma Z. Wagnerite-Ma5bc, a new polytype of $Mg_2(PO_4)(F,OH)$, from granulite-facies Paragneiss, Larsemann Hills, Prydz Bay, East Antarctica. Can Mineral. 2003;41:393–411. doi:10.2113/GSCANMIN.41.2.393

54. Duan H, Du K, Yan C., Wang F. Electrochemical corrosion behavior of composite coatings of sealed MAO film on magnesium alloy AZ91D. Electrochim Acta. 2006;51:2898–2908. doi:10.1016/j.electacta.2005.08.026

55. Hwang DY, Kim YM, Shin DH. Corrosion resistance of plasma-anodized AZ91 Mg alloy in the electrolyte with/without potassium fluoride. Mater Trans. 2009;50:671–678. doi:10.2320/MATERTRANS.MER2008345

56. Lujun Z, Hongzhan H, Qingmei M, Jiangbo L, Zhengxian L. The mechanism for tuning the corrosion resistance and pore density of plasma electrolytic oxidation (PEO) coatings on Mg alloy with fluoride addition. J Magnes Alloy. 2021. doi:10.1016/J.JMA.2021.10.007

57. Chen Q, Zheng Y, Dong S, Chen XB, Dong J. Effects of fluoride ions as electrolyte additives for a PEO/Ni-P composite coating onto Mg alloy AZ31B. Surf Coatings Technol. 2021;417:126883. doi:10.1016/j.surfcoat.2021.126883